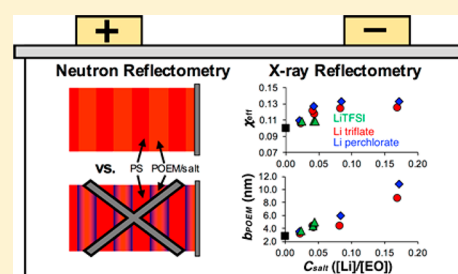


Quantifying Lithium Salt and Polymer Density Distributions in Nanostructured Ion-Conducting Block Polymers

Thomas E. Gartner, III,[†] Melody A. Morris,[†] Cameron K. Shelton,[†] Joseph A. Dura,[§] and Thomas H. Epps, III^{*,†,‡,§}[†]Department of Chemical & Biomolecular Engineering and [‡]Department of Materials Science & Engineering, University of Delaware, Newark, Delaware 19716, United States[§]NIST Center for Neutron Research, National Institute of Standards and Technology, Gaithersburg, Maryland 20899, United States

Supporting Information

ABSTRACT: Block polymer (BP) electrolytes offer significant advantages relative to existing liquid or polymer electrolytes due to their independently tunable ion transport and mechanical stability properties as a result of nanoscale self-assembly. Many of these nanostructured electrolytes are composed of a BP that is doped with a lithium salt to impart conductivity but which also alters the self-assembly (structure and thermodynamics) in comparison to the neat BP. By elucidating the effects of lithium salt concentration and counterion chemistry on the relevant salt and polymer density distributions, BP electrolytes with more efficient conductivity pathways can be developed. In this work, neutron and X-ray reflectometry (NR and XRR, respectively) were harnessed to determine the spatial distribution of salt and polymer in lamellae-forming polystyrene-*block*-poly(oligo-oxyethylene methacrylate) [PS-*b*-POEM] films doped with various lithium salts. From the NR results, the distribution of lithium salts across domains appeared to match that of the POEM in the BP electrolyte for all salts tested. This finding of a salt distribution that was directly proportional to the POEM density profile facilitated quantitative analysis of polymer and salt XRR profiles using a strong-segregation theory framework. Through this approach, effective Flory–Huggins interaction parameters (χ_{eff})s were deconvoluted from POEM statistical segment lengths (b_{POEM})s. For all salts tested, χ_{eff} increased at low salt concentrations and then plateaued at higher salt concentrations, while b_{POEM} increased linearly across all salt concentrations. These findings can be leveraged to advance the next generation of salt-doped BP electrolyte materials that enhance the performance and mechanical stability of lithium-ion batteries.



INTRODUCTION

With the increasing global requirements for energy generation and storage, lithium-ion batteries are attractive devices for numerous applications because of their inherently high energy density and ability to be recharged.^{1–4} In most commercialized lithium-ion batteries, the electrolyte system is composed of a flammable liquid electrolyte and a thin polymer separator membrane. This liquid/separator configuration is susceptible to dendrite penetration, and catastrophic failures in the associated battery systems can occur if the separator ruptures.^{4–6} Homopolymer electrolytes, typically composed of poly(ethylene oxide) [PEO] doped with a lithium salt to provide conductivity, can mitigate the concerns with flammability but fail to arrest the lithium dendrite formation that can cause short-circuiting and device failure.^{7–9}

As an alternative to homopolymer-based polymer electrolytes, block polymer (BP) electrolytes can be designed to independently address the competing ion transport and mechanical robustness metrics, while maintaining ease of processing, all in a single material.^{8,10–13} For example, the archetypal BP electrolyte is a lithium salt-doped polystyrene-*block*-PEO (PS-*b*-PEO), in which the PS block provides mechanical strength due to its high glass transition temperature and relatively high elastic modulus, while the PEO block

promotes high lithium-ion conductivity.^{14,15} As a result of the nanostructured domains of the BP, the ionic conductivity and modulus are decoupled, enabling the independent optimization of both properties through alterations in block chemistry, block sequence, or chain architecture.^{16–18} Though there is a reasonable understanding of neat BP nanostructure and self-assembly,^{19–22} the holistic impact of lithium salt addition on BP self-assembly, chain dimensions, and energetics remains unclear, making optimization of BP electrolyte systems a challenging endeavor. Thus, due to the intricacies of BP and lithium salt interactions, it is essential to gain further quantitative information with respect to the distribution of salts in BP domains and the corresponding effect of salt (counterion and concentration) on the BP domain spacings, interfacial widths, statistical segment lengths, and effective interactions.

Though it is common that lithium salts preferentially segregate into the ion-conducting domains,²³ various reports have provided differing results regarding the ion distributions within that solvating domain.^{24–26} For example, Gomez et al.

Received: December 7, 2017

Revised: February 5, 2018

Published: February 22, 2018

used energy-filtered transmission electron microscopy to image the lithium distribution in lamellar lithium bis-(trifluoromethane)sulfonimide (LiTFSI)-doped PS-*b*-PEO BP electrolytes and reported that the lithium tended to localize into the center of the PEO domains, which became more apparent with increased PS-*b*-PEO molecular weight.²⁴ The localization of the salt was attributed to inhomogeneous local stress fields in the BP domains as calculated by self-consistent field theory for a neat BP.²⁴ Other work using X-ray photoelectron spectroscopy (XPS) with C₆₀⁺ etching examined lithium trifluoromethanesulfonate (Li triflate)-doped PS-*block*-poly(oligo-oxyethylene methacrylate) [PS-*b*-POEM], in which the conducting block (POEM) consisted of short PEO side chains attached to a methacrylate backbone.²⁵ Quantitative composition profiles were determined, which suggested that the lithium content was directly proportional to the POEM concentration across each lamellar domain.²⁵ Several theory/simulation efforts have reported conclusions similar to the XPS data, in which the distribution of the salt closely follows the distribution of the solvating polymer across domains.^{26,27} Because conductivity is highly dependent on lithium salt concentration and counterion,²⁸ gaining a complete understanding of the local concentration of salt in a BP electrolyte is essential.²⁹ Furthermore, by correlating the salt and polymer distributions, the physical properties of the polymer electrolyte system can be pre-designed to maximize lithium ion transport behavior.

In addition to mapping the spatial distribution of salt within the BP, the successful design of nanostructured BP electrolyte materials necessitates an understanding of how salt loading impacts the thermodynamics of BP self-assembly. Several reports indicate that lithium salt addition increases the effective Flory–Huggins interaction parameter (χ_{eff}) between the polymer blocks as well as the stiffness (i.e., statistical segment length, b) of the chains comprising the ion-conducting domain.^{26,30–38} Early studies suggested a linear relationship between χ_{eff} and salt concentration.^{30,31} For example, strong-segregation theory (SST)^{39,40} was used to link the BP domain spacing (L_0)^{41–43} to the χ_{eff} for salt-doped PS-*b*-PEO, under the assumption of a near-constant b , and that approach determined a linear increase in χ_{eff} with salt concentration.³⁰ However, recent experimental work has presented a nuanced picture of χ_{eff} as a more complex function of both molecular weight and salt concentration,^{36,44} which theoretical work suggested may be due to incomplete dissociation of the salt.⁴⁵ Thus, a more complete picture of the combined effects of the increase in χ_{eff} and chain stiffness is desired to improve understanding of polymer/salt cooperative assembly.

Herein, we determined lithium salt and BP density profiles of nanostructured electrolytes to deconvolute parameters such as χ_{eff} and the b of the conducting block as a function of salt loading. To elucidate the effects of salt doping on BP thermodynamics and self-assembly, we probed the spatial distributions of both the lithium ions and polymers in the PS-*b*-POEM system upon the addition of three different salts (LiTFSI, Li triflate, and Li perchlorate). Lithium salt distributions were examined using neutron reflectometry (NR) by leveraging the natural contrast between the lithium salt (higher scattering length density [SLD] than PS) and POEM (lower SLD than PS). Though the direct determination of the details of lithium distributions within a thin layer normally is challenging using this approach,⁴⁶ we harnessed the contrast matching behavior⁴⁷ that occurs as a function of salt

loading to infer uniform salt segregation behavior.^{48,49} For example, if the lithium salt was distributed proportionally across the POEM domains (i.e., at a constant ratio relative to the local POEM content), one would expect that the SLD of the entire doped POEM domain would increase and proportionally decrease the contrast between the PS and POEM/salt layers. Whereas, if the salt preferentially localized in the center of the POEM domains, one would expect a high-salt-concentration (high SLD) domain of POEM sandwiched between two lower-salt-concentration (low SLD) domains of POEM. At the salt-doping ratios and molecular weights tested, the NR results suggested an even distribution of salt for all three counterions, as described below.

The spatial distributions of polymer were studied with X-ray reflectivity (XRR) because of the inherent contrast between the PS and POEM domains under X-rays. BP L_0 s and interfacial widths (t_{int})s were determined as a function of salt concentration and counterion chemistry to track the effects of salt loading on domain structure. This information was used to determine the dependence of χ_{eff} and the b of the POEM domain (b_{POEM}) on salt concentration via an SST approach.^{43,50} The SST analysis revealed that as salt concentration increased, χ_{eff} increased up to a point and then plateaued (in agreement with literature³⁶), while b_{POEM} increased linearly at all salt concentrations and appeared to be the predominant contributor to the increase in L_0 . In total, this combined NR and XRR analysis was able to deconvolute the various effects of BP lithium salt doping on BP electrolyte thermodynamics and self-assembly, which will facilitate the design and manufacture of better BP electrolytes.

■ MATERIALS AND METHODS

Materials. Styrene (99%, stabilized, Acros Organics) and oligo-oxyethylene methacrylate (OEM, >99%, stabilized, Sigma-Aldrich, average molar mass = 475 g mol⁻¹) were purified by passage through basic alumina columns. Styrene was dried further by distillation from calcium hydride. Both styrene and OEM were degassed via three freeze–pump–thaw cycles and then transferred into an argon-filled glovebox prior to use. Propargyl 2-bromoisobutyrate (PgBiB) was synthesized according to literature procedures (yield ≈80%).⁵¹ Copper bromide [Cu(I)Br, 98%, Acros Organics] was purified by stirring in acetic acid for 30 min, filtering, washing two times with cold ethanol, and drying under dynamic vacuum; after purification, it was stored in an argon-filled glovebox. Anhydrous methanol (99.8%, Sigma-Aldrich) was degassed via three freeze–pump–thaw cycles, stirred with calcium hydride overnight, and distilled prior to being stored in an argon-filled glovebox. *N,N,N',N'',N'''*-Pentamethyldiethylenetriamine (PMDETA, 99%, Sigma-Aldrich), tetrahydrofuran (THF, >99%, optima, Fisher Scientific), and anisole (>99%, Fisher Scientific) were degassed via three freeze–pump–thaw cycles prior to storing in an argon-filled glovebox.

Polymer Synthesis and Characterization. PS-*b*-POEM was synthesized according to literature protocols.⁵² The molecular weight of the PS block and the dispersity of the PS-*b*-POEM were determined using a Viscotek VE2001 size-exclusion chromatography (SEC) instrument with THF as the eluent (1.0 mL/min) and polystyrene standards (1780–205 000 g/mol) as reference. The relative volume fractions of the blocks were determined via proton nuclear magnetic resonance (¹H NMR, Bruker AV400) spectroscopy with CDCl₃ (0.03% v/v TMS) as a solvent. The PS-*b*-POEMs and all lithium salts were dried under dynamic vacuum at elevated temperature (120 °C for the polymer and 150 °C for the salts) for at least 24 h prior to transfer into an argon glovebox for storage and sample preparation.

Polymer Film Preparation. PS-*b*-POEM and Li triflate, Li perchlorate, and LiTFSI salt stock solutions were prepared by dissolving each material separately in THF at approximately 5 wt %

and then stirring overnight. Next, the appropriate polymer and salt stock solutions were mixed at varying gravimetric ratios and stirred for another 4–6 h. The salt concentration was quantified in all samples as the ratio [EO]:[Li], which represents the molar ratio of ethylene oxide monomer segments in the side chains of POEM to the number of lithium ions doped into the BP. Approximately 15 wt % methanol was added to the polymer/salt solutions to promote PS-*b*-POEM and lithium salt dissolution and mixing, which resulted in higher-quality thin films. Final polymer/salt/THF/methanol solutions were ~3.5 wt % polymer.

Silicon wafer substrates (Wafer World Inc.) were rinsed three times with toluene and cleaned in an ultraviolet-ozone oven (model 342, Jelight Co., Inc.). All polymer films were cast on the cleaned silicon substrates via flow coating.⁵³ For NR experiments, 64 mm long, 25.4 mm wide PS-*b*-POEM films with uniform thicknesses (ranging from 100 to 180 nm depending on the salt and salt concentration; 3.5 repeat domains total for all NR samples) were cast using PS-*b*-POEM sample I ($M_n = 53\,900$ g/mol, $f_{\text{POEM}} = 0.50$, $M_w/M_n = 1.22$). For XRR experiments, gradient thickness films (70 mm long, 25.4 mm wide, and between ~90 and ~140 nm thick) were prepared using PS-*b*-POEM sample II ($M_n = 60\,000$ g/mol, $f_{\text{POEM}} = 0.44$, $M_w/M_n = 1.10$). XRR was performed, orthogonal to the gradient direction, on sections of the films of thickness commensurate to the L_0 (2.5, 3.5, or 4.5 lamellar periods depending on the particular film). Prior to NR or XRR, all films were subjected to dynamic vacuum overnight at room temperature followed by annealing under dynamic vacuum for 6 h at 135 °C. Film thicknesses were measured using a Filmetrics F20-UV interferometer operated in reflectance mode.

Neutron Reflectometry. NR experiments were conducted using the multiangle grazing-incidence k-vector (MAGIK) instrument at the National Institute of Standards and Technology (NIST) Center for Neutron Research.⁵⁴ Neutrons with an incident wavelength of 5 Å were directed at the neat and salt-doped PS-*b*-POEM films. For each sample, Q_z scans (0–0.0877 Å⁻¹) were recorded with a step size of 0.0004 Å⁻¹. Films were held in the neutron beam in a reflectivity geometry using an aluminum sample holder and elastic clamps. The elastic clamps secured the substrate to a base plate with minimal force in comparison to metal clamps, thereby reducing any warping of the silicon substrates (~0.5 mm thick). A borated aluminum mask was placed between the neutron source and films to prevent neutrons from scattering off the holder, clamp, and portions of the silicon wafers not coated with film. The resulting reflectometry profiles were reduced using reflred software according to standard protocols⁵⁵ and analyzed with repeating lamellae models in the reflfit and refl1D software programs.^{56,57} During the fitting procedure, the thickness and SLD of each PS and POEM layer were allowed to vary independently. The SLD of the SiO₂ layer at the polymer–substrate interface was fixed at the bulk value (3.5×10^{-6} Å⁻²), and the SiO₂ layer thickness was allowed to vary from 5 to 15 Å. The reflfit and refl1D programs also were used to generate predictive fits prior to performing the NR experiments as described in the Results section.

X-ray Reflectometry. XRR experiments were conducted on a Rigaku Ultima IV X-ray diffractometer. A 5 mm wide parallel beam of Cu K α radiation ($\lambda = 0.154$ nm) was scanned over incident angles (θ) and detection angles (2θ) of $0^\circ < 2\theta < 3^\circ$ with a step size of 0.004° at a scan rate of $0.5^\circ \text{ min}^{-1}$. The films had an estimated 2 nm thickness gradient across the beam width, which was on the order of the roughness of the top surface of the films. Rigaku Globalfit software was used to fit the recorded XRR profiles with horizontal layer models. A wetting layer of POEM was modeled at the substrate–polymer interface, a capping layer of PS was modeled at the polymer–air interface, and alternating layers of PS and POEM were modeled in-between.²⁵

Atomic Force Microscopy (AFM). A Veeco Dimension 3100 operating in tapping mode was used to capture AFM images of the top surface of the PS-*b*-POEM films. Silicon probes (Tap150G, Budget-Sensors) were used with a typical set point ratio of 0.75.

RESULTS AND DISCUSSION

Characterization of the spatial distributions of the salt and polymer species provides information about the effect of lithium salt addition on the BP interactions and chain conformations, and it helps identify methods to tune electrolyte nanostructures and target desired local salt concentrations. To this end, the tailored application of scattering techniques to these systems is essential to probe salt and polymer distributions and achieve quantitative results. In this section, we first present the NR results, followed by a discussion of how we inferred the salt distributions in PS-*b*-POEM films from the obtained NR profiles. Next, we present the XRR results, followed by a discussion of how we determined polymer domain characteristics and thermodynamics from the calculated XRR fits.

Neutron Reflectometry Results. The neutron and X-ray scattering length densities of the materials used in this study are listed in Table 1. Because all the lithium salts had higher SLDs

Table 1. Neutron and X-ray Scattering Length Densities⁵⁸

	polymer		salt		
	PS	POEM	LiTFSI	Li triflate	Li perchlorate
X-ray scattering length density ($\times 10^6$ Å ⁻²)	9.61	11.30	16.91	15.86	20.30
neutron scattering length density ($\times 10^6$ Å ⁻²)	1.41	0.78	3.55	3.08	4.23

than POEM, the addition of salt to the POEM domains increased the total SLD of the combined POEM/salt layers ($\rho_{\text{POEM/salt}}$), as described by eq 1

$$\rho_{\text{POEM/salt}} = \rho_{\text{POEM}}(1 - \phi_{\text{salt}}) + \rho_{\text{salt}}\phi_{\text{salt}} \quad (1)$$

in which ϕ_{salt} is the volume fraction of salt in the POEM/salt domain. The increasing $\rho_{\text{POEM/salt}}$ progressively reduced the overall scattering contrast between the PS and POEM/salt domains as the salt concentration increased. The salt concentration at which $\rho_{\text{POEM/salt}}$ was equal to ρ_{PS} was defined as the contrast match point; at this contrast matched salt concentration the salt-doped films had a nearly uniform SLD as a function of depth in the films. We note that eq 1 depends on the assumption of ideal mixing between polymer and salt. This assumption may result in slight deviations between the contrast match salt concentrations obtained from the NR results and the expected concentrations derived from eq 1.

NR profiles of the neat PS-*b*-POEM film and films doped with [EO]:[Li] ratios of 45:1, 22:1, and 11:1 [black data points, Figure 1] were collected on the MAGIK reflectometer. As the salt concentration increased, the Bragg peak locations (marked with yellow arrows) shifted to lower Q_z values, which reflected an increase in the L_0 s of the films upon salt addition. Notably, Bragg peaks were not present in the LiTFSI-doped PS-*b*-POEM film at an [EO]:[Li] ratio of 11:1, which indicated that the contrast matched salt concentration was reached for that film.

The NR profiles were fit with multilayer lamellae models to obtain SLD as a function of position in the films. The NR profiles, fits, and SLD profiles for PS-*b*-POEM films doped with LiTFSI are shown in Figure 2. Multilayer model fits for the PS-*b*-POEM films doped with Li triflate and Li perchlorate are included in the Supporting Information (Figures S1 and S2). As

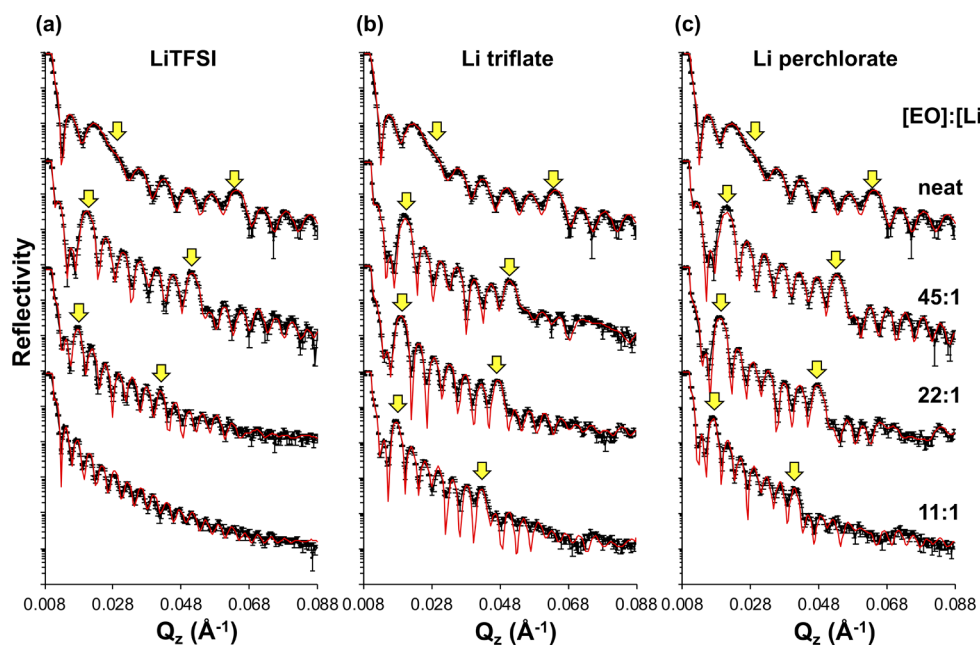


Figure 1. NR profiles (black data points) and model fits (red lines) of the neat PS-*b*-POEM film (top profiles) and films doped at [EO]:[Li] ratios of 45:1, 22:1, and 11:1 with (a) LiTFSI, (b) Li triflate, and (c) Li perchlorate salts. Bragg peaks (marked by yellow arrows) shifted to smaller Q_z values as the salt concentration increased (from top to bottom in the profiles). Bragg peaks were not noticeable in the LiTFSI film doped with an 11:1 [EO]:[Li] ratio. Error bars represent one standard deviation from the measured intensity and were calculated during data reduction.

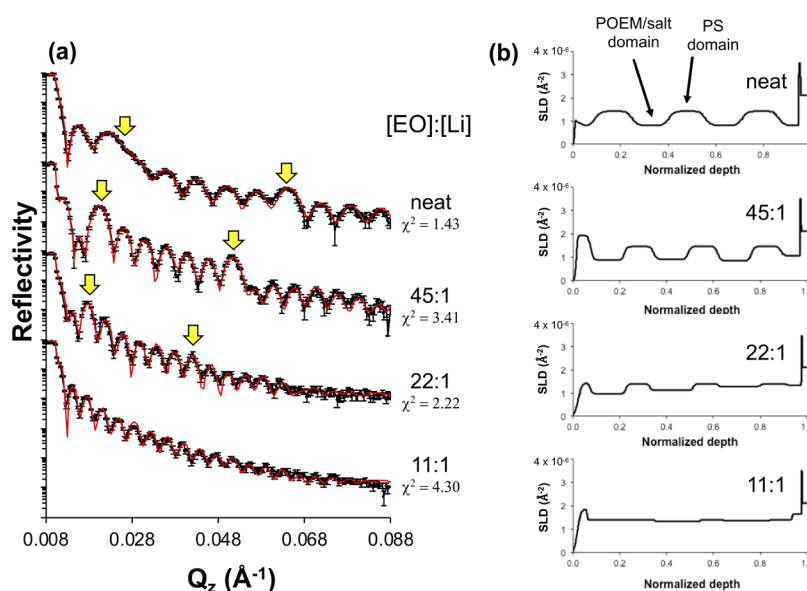


Figure 2. (a) NR profiles (black data points) and model fits (red lines) for the neat PS-*b*-POEM film and films doped with LiTFSI at 45:1, 22:1, and 11:1 [EO]:[Li] ratios (profiles from Figure 1) and (b) SLD profiles as a function of film depth (normalized from zero [free surface] to one [substrate surface]). As the salt concentration in the film increased, $\rho_{\text{POEM/salt}}$ increased toward ρ_{PS} until a contrast matched point ($\rho_{\text{POEM/salt}} \approx \rho_{\text{PS}}$) was achieved at [EO]:[Li] \approx 11:1. Bragg peaks (marked by yellow arrows) were not present at the 11:1 ratio. Furthermore, SLD models indicated a minor change in salt concentration in the POEM layers from the free to substrate surface. Error bars in NR profiles represent one standard deviation from the measured intensity and were calculated during data reduction; the χ^2 values in panel (a) are a measure of the quality of the fits, as output from the refl1D software. We note that the statistical χ^2 reported in this figure is not related to the Flory–Huggins χ_{eff} discussed elsewhere in the paper.

a result of differences in total film thickness between samples (the presence of salt swelled the POEM domains), the SLD profiles are plotted as a function of normalized depth, ranging from 0.00 (free surface) to 1.00 (substrate surface). For all samples, the ρ_{PS} values did not change from that of neat PS (i.e., the salt did not appear to penetrate, or otherwise alter, the PS domains), in agreement with the literature.^{24–26} However,

the $\rho_{\text{POEM/salt}}$ values increased with salt concentration due to solvation of the lithium ions in the POEM domains. This behavior reflected a reduction in contrast between PS and POEM/salt domains as salt was added. At an [EO]:[Li] of 11:1 for the LiTFSI samples, the model fits indicated that $\rho_{\text{POEM/salt}}$ was approximately equal to ρ_{PS} , which resulted in the disappearance of the Bragg peaks in the NR profile. The

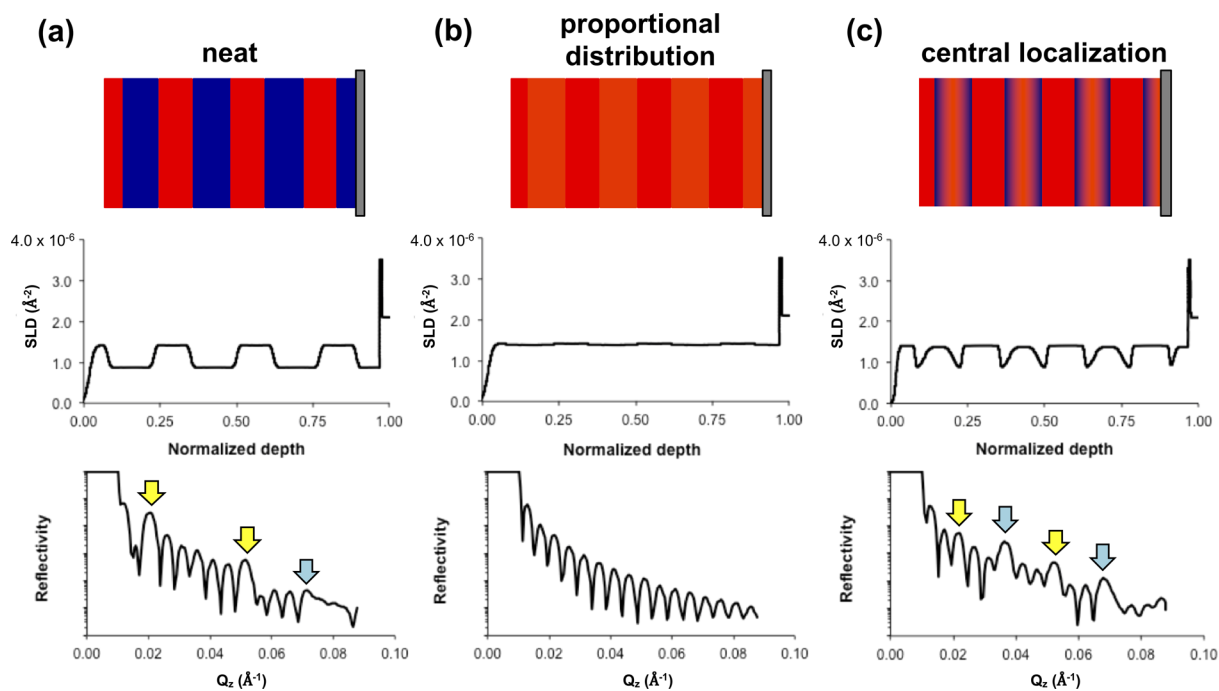


Figure 3. Representations of neutron contrast between PS (red) and POEM (blue) domains (top row) (a) in a neat PS-*b*-POEM film and if lithium salt distributed (b) proportionally through the POEM domains or (c) preferentially in the center of POEM domains at the contrast match point. Key differences between the three conditions are indicated in modeled SLD (middle row) and reflectivity (bottom row) profiles. Modeled SLD profiles are plotted as a function of normalized depth such that 0.00 is the free surface and 1.00 is the substrate surface (middle row). Odd-order Bragg peaks in the reflectivity profiles are marked with yellow arrows, and even-order Bragg peaks are marked with blue arrows. Neat (no salt) samples (a) result in primarily odd-order Bragg peaks (bottom row). Even distributions of salt within the POEM layers (b) result in reflectivity profiles with no Bragg peaks (bottom row). Central localizations of the salt within the POEM layers (c) result in both odd- and even-order Bragg peaks (bottom row).

average contrast between PS and POEM/salt domains as obtained from the model fits is plotted in Figure S3. Of note is the lack of SLD change between neat POEM and POEM/salt domains at low salt concentrations—this behavior was a result of the mass density decrease of the POEM/salt domains (see Table S1) balancing out the scattering length contribution of the salt. Once the salt concentration increased further (greater than $C_{\text{salt}} = [\text{Li}]/[\text{EO}] = 0.025$), the overall $\rho_{\text{POEM/salt}}$ began to increase as expected.

Discussion: Determining Salt Distribution from NR Profiles. Utilizing the pronounced impacts of the differences in symmetries between uniformly distributed and localized salt contents on the NR profiles (particularly as the average composition approached the contrast matched point), we characterized the salt distribution within the POEM layers as demonstrated by the theoretical NR profiles in Figure 3. In a neat sample (Figure 3a), the NR profile should contain only odd-order Bragg peaks due to reflections from the repeating two-layer PS and POEM structure (because the Bragg peaks represent the square of the Fourier components of the SLD depth profile). In this model, the PS and POEM/salt layers are of nearly equal thickness, resulting in an approximately symmetric structure that suppresses the even-order Bragg peaks.⁵⁹ In a film doped to the contrast-matched salt concentration, if the local salt concentration was directly proportional to the POEM concentration (Figure 3b), $\rho_{\text{POEM/salt}}$ would be approximately equal to ρ_{PS} . Therefore, the resulting NR profile would contain Kiessig fringes (related to film thickness) but no Bragg peaks (related to the presence of repeating multilayers) due to the lack of contrasting SLD in the layers throughout the film. However, if the salt was localized to the middle of the POEM layers (Figure 3c), neutrons would

scatter from all interfaces in the film, including the top surface of the film, the substrate, each PS/POEM interface, and each interface between regions of high vs low salt concentration (i.e., high SLD vs low SLD) near the center of the POEM domains. The resulting NR profile would contain Kiessig fringes and both even- and odd-order Bragg peaks as a result of interference from a periodic structure lacking low-order commensurability.⁵⁹ These easily recognizable differences in the number of apparent Bragg peaks between different salt localizations demonstrate the capability of neutron scattering to infer additive distributions in thin films.

A comparison between the measured NR profiles (Figures 1 and 2) and the theoretical NR profiles (Figure 3) allowed the inference of the spatial distribution of salt in the films. In all samples, the lack of even-order Bragg peaks suggested that the salt concentration was roughly proportional to the POEM concentration (i.e., the salt distribution mirrored the POEM distribution within the domains). Furthermore, the complete lack of Bragg peaks in the 11:1 LiTFSI film provided further evidence that the salt distribution both followed the POEM domain profile and that the $\rho_{\text{POEM/salt}}$ was contrast-matched to the ρ_{PS} , in agreement with the theoretical picture in Figure 3b. Complete disappearance of Bragg peaks in the Li triflate and Li perchlorate samples did not occur for the salt concentrations studied herein because higher salt doping levels were necessary to reach the contrast match condition for those salts primarily because of their smaller molar volumes. For example, $\rho_{\text{POEM/salt}}$ calculations using eq 1 (see the Supporting Information, section S1) indicated that the contrast match point was expected at LiTFSI, Li triflate, and Li perchlorate [EO]:[Li] ratios of 13:1, 6:1, and 5:1, respectively, in rough agreement with the extrapolated contrast match points shown in Figure S3. Small

deviations between the expected contrast match conditions from eq 1 and the extrapolated contrast match points from Figure S3 may be explained by the assumptions inherent in eq 1 as discussed above. However, we note that all other analyses in this work depended only on the measured $\rho_{\text{POEM/salt}}$ on the basis of the NR results and were independent of the ideal mixing assumptions used in eq 1.

NR profiles for salt concentrations higher than 11:1 are not reported, as the PS-*b*-POEM I BP used for the NR study had a morphological transition from lamellae to cylinders at [EO]:[Li] ratios near 6:1. For films that exhibited a morphology change, a lack of Bragg peaks in the NR profile would not necessarily be indicative of the contrast matched condition because the disappearance of Bragg peaks could simply be due to the disruption of the repeating layer structure as a result of the morphology transition. Because the LiTFSI sample did not exhibit a morphology transition at the expected contrast match condition ([EO]:[Li] \approx 11:1) and because the contrast extrapolated to zero at roughly this composition (see Figure S3), we can suggest that the lack of Bragg peaks for this lamellar sample is a strong indicator of a contrast matched condition.

In addition to inferring the distribution of salt in each POEM domain, we used the layer model fits to determine the changes in salt concentration as a function of depth in the films. On the basis of the modeled SLD profiles (Figure 2b, Figures S1b and S2b), we noted a possible segregation of salt to the polymer–substrate and polymer–air interfaces, though the results were not conclusive. This phenomenon has been discussed in the literature for PS-*b*-PEO films doped with LiTFSI.⁶⁰

X-ray Reflectometry Results. Because NR did not have the range in Q_z to quantitatively determine the interfacial roughnesses between the PS and POEM domains, XRR was employed to measure the detailed structural characteristics of the films as a function of salt content. The slightly asymmetric PS-*b*-POEM II ($f_{\text{POEM}} = 0.44$) was used for XRR experiments to allow high salt concentrations to be interrogated while still maintaining a lamellar morphology. The measured XRR profiles and fits for the neat PS-*b*-POEM II and for samples mixed with LiTFSI, Li triflate, and Li perchlorate salts at [EO]:[Li] = 48:1, 24:1, 12:1, and 6:1 are plotted in Figure S4. The L_0 and volume fraction of interface (f_{int}) for each layer were obtained via fitting horizontal layer models to the XRR profiles, and the results are plotted in Figures 4a and 4b, respectively. The L_0 increased approximately linearly over the salt concentrations studied as a result of the swelling of the POEM domains upon the addition of salt, but the slope of this increase was a function of counterion chemistry. LiTFSI-doped films had the largest L_0 at a given salt concentration, while Li triflate-doped films had the smallest L_0 . Similar to the behavior noted in the literature for a variety of PEO-based BPs, the amount of swelling of the POEM domains deviated significantly from what would be expected from a simple assumption of ideal mixing due to the salt-induced stretching of the POEM blocks.^{30,36,37,61} For XRR analyses, LiTFSI films are reported only for [EO]:[Li] ratios greater than [EO]:[Li] = 12:1, as the 12:1 LiTFSI film showed competition between lamellae and cylinders, and the 6:1 LiTFSI films displayed a cylindrical morphology. AFM images supporting these morphology assignments are presented in Figure S5.

The f_{int} (see Figure 4b) is defined as twice the average t_{int} between PS-rich and POEM-rich domains, normalized by the L_0 , and represents the fractional volume of each lamellar period encompassed by the interfacial region between the domains:

$$f_{\text{int}} = \frac{2t_{\text{int}}}{L_0} = \frac{2(2\pi)^{1/2}\delta}{L_0} \quad (2)$$

in which δ is the average roughness parameter obtained via the Rigaku GlobalFit software.^{62–64} The f_{int} decreased with increasing salt content, reflecting an increase in the effective segregation strength between the PS and POEM domains as salt was added. However, at high salt concentrations (24:1 in the LiTFSI film and 6:1 in the Li triflate and Li perchlorate films), the interfacial roughness increased to a value comparable to, or higher than, the neat film.

Domain composition profiles also were obtained from the XRR fits, in which the interfacial profiles were modeled as an

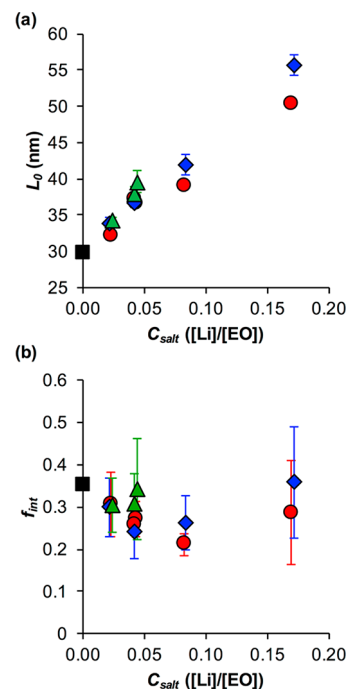


Figure 4. (a) Domain spacing, L_0 , and (b) volume fraction of interface, f_{int} , as a function of lithium salt concentration, C_{salt} , for three counterions: TFSI (green triangles), triflate (red circles), and perchlorate (blue diamonds). L_0 increased with increasing salt concentration for all counterions, whereas f_{int} decreased at low salt concentrations before a slight increase at high salt concentrations. The error bars in panel (a) are the standard deviation in layer thickness obtained from the XRR fits, and the error bars in panel (b) are propagated uncertainties based on the standard deviation of the thickness and roughness parameters obtained from the XRR fits. For cases in which the error bars are not visible, the error is smaller than the size of the data point.

error function using the average PS and POEM layer thickness and roughness parameters.⁶² The volume fraction of POEM (ϕ_{POEM}) as a function of position across one lamellar period (z) is plotted in Figure 5 for each salt and salt doping ratio. The volume fraction of PS (ϕ_{PS}) as a function of z is plotted in Figure S6. The composition profiles reflected the trends reported in the L_0 and f_{int} data above, in that the POEM-rich domain swelled with increasing C_{salt} and the interfacial profiles sharpened at intermediate C_{salt} (evidenced by the increased slope of the composition profiles). However, increased mixing between domains occurred at high salt concentrations ([EO]:[Li] = 24:1 for LiTFSI, 6:1 for Li triflate, and 6:1 for Li perchlorate). All salt-doped lamellar specimens had PS and

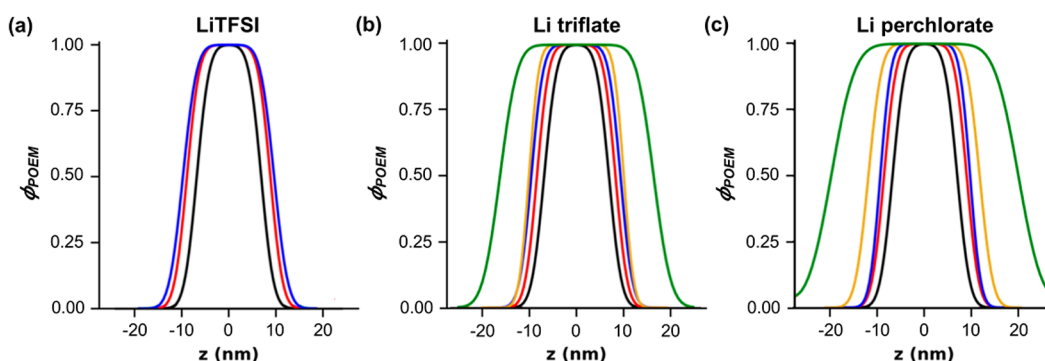


Figure 5. Volume fraction of POEM (ϕ_{POEM}) as a function of location (z) across one lamellar period for films doped with (a) LiTFSI, (b) Li triflate, and (c) Li perchlorate. The POEM domains are centered at $z = 0$, with each curve extending to $z = \pm L_0/2$. The color of the profiles corresponds to the salt-doping level: neat (black); [EO]:[Li] = 48:1 (red); 24:1 (blue); 12:1 (goldenrod); or 6:1 (green).

POEM domains with high purity (i.e., $\phi_{\text{POEM}} > 0.999$ at the peak of the composition profiles), indicating that the strong-segregation limit was a reasonable approximation for these films.⁴¹

Discussion. Domain Characteristics and Salt-Mediated Thermodynamics from X-ray Reflectometry. The XRR results highlighted the changes in the thin film domain characteristics (L_0 s and t_{int} s) as a function of salt concentration and counterion choice, and we leveraged these results to examine how salt addition impacts the polymer–polymer interactions and chain stiffnesses. In Figure 4a, we demonstrated a linear increase in L_0 as salt as added (due to lithium ions interacting with the PEO side chains of the POEM, increasing the chain stiffness) and that the slope of L_0 vs salt concentration was highest for LiTFSI, followed by Li perchlorate, and then Li triflate. We attributed this trend to competition between two factors which have been discussed previously in the literature: (1) the Lewis basicity of the counterion³⁰ and (2) the size of the counterion.³² Our XRR results confirmed that these trends obtained in the literature for bulk BP samples also hold in the thin film geometry. In Figure 4b, we demonstrated that f_{int} displayed small differences as a function of counterion choice, though these differences were on the order of the uncertainty in the data. After an initial decrease in f_{int} in comparison to the neat sample, all salts showed an increase in f_{int} at high salt concentrations. This phenomenon likely was a result of the highly salt-doped films approaching the lamellar \rightarrow cylinder morphology transition due to swelling of the POEM domains. As the films neared this transition, buckling of the lamellae induced the increase in interfacial roughness noted in the XRR data.

We analyzed the XRR results within the context of SST for conformationally asymmetric polymers to determine how salt altered chain stretching and mediated polymer–polymer interactions. The SST framework was used, which provided expressions for L_0 ^{41–43} and t_{int} ^{50,65–67} as a function of χ and chain characteristics through parameters such as the degree of polymerization (N) and b , in the limit of strong segregation between the polymer blocks ($\chi N > 50$). We used the L_0 , t_{int} , and domain density information obtained from the XRR fits to calculate the χ_{eff} and the b_{POEM} as a function of salt content. Full specifics of the SST calculation are given in the Supporting Information section S2, but relevant aspects are reported here. The SST derivations found in the literature provided expressions for the L_0 ⁴³ and t_{int} ⁵⁰ as a function of χ (or in this case χ_{eff}), N , and the volume fractions, densities, and b of

the components. The L_0 , t_{int} , and domain density information from XRR were input into the SST expressions, which then were solved simultaneously to yield the χ_{eff} (Figure 6a) and b_{POEM} (Figure 6b). For these calculations, the b of PS was assumed to be constant at $b_{\text{PS}} = 0.68$ nm, with a reference volume $\nu_0 = 0.668$ nm³ (the volume of one POEM monomer).

The χ_{eff} between PS and POEM increased with increasing salt concentration, with the counterion impacting the value of the plateau of the χ_{eff} curve. Li perchlorate had the lowest Lewis basicity of the three counterions and exhibited the largest increase in χ_{eff} , while the LiTFSI had the highest Lewis basicity and exhibited the smallest increase in χ_{eff} . The changes in χ_{eff} qualitatively matched the results of Teran and Balsara,³⁶ despite some differences between the system and characterization methods (they used the random-phase approximation (RPA) to determine χ_{eff} from SAXS patterns from low molecular weight, disordered PS-*b*-PEO samples). Also, the value of χ for neat PS–POEM was close to that obtained in the literature,^{52,68} though the previous values for χ were obtained either at a much higher temperature (by RPA)⁵² or for shorter PEO side chains.⁶⁸ Notably, the b_{POEM} increased dramatically with increasing salt content, and this increase was approximately linear over the salt concentrations studied. Thus, it is apparent that the stiffening of the POEM polymer (and a corresponding decrease in effective segment density) is a major contributor to the increase in L_0 with the addition of Li salt, rather than solely the result of changing effective interactions as modeled in prior work.³⁰ A comparison between the SST analysis presented here, in which both χ_{eff} and b_{POEM} change with salt content, and the SST analysis of ref 30, in which b_{POEM} was assumed constant, is given in Figure S7.

Overall, the XRR results provided insight into the effects of the lithium salt on the structure and thermodynamics of the PS-*b*-POEM BP. By interrogating a systematic parameter space of lithium counterion and salt concentration, we obtained a more detailed mapping between salt doping and the BP L_0 , t_{int} , χ_{eff} , and chain stretching/stiffness. We applied an SST analysis which enabled decoupling of χ_{eff} from b_{POEM} and revealed that χ_{eff} plateaued at higher salt concentrations whereas b_{POEM} increased linearly with increasing salt concentration. Furthermore, the salt-doped BPs exhibited increased L_0 and decreased t_{int} with increasing salt loading. Lower basicity counterions (e.g., Li perchlorate) had a stronger effect on the considered BP characteristics, with the exception of the L_0 which also was sensitive to the size of the counterion, demonstrating that similar trends discussed in the literature for salt-doped bulk BP

systems also are valid for salt-doped thin films. We note that the above XRR analysis was predicated on our inference from NR that the local salt concentration was essentially proportional to the POEM concentration. This salt distribution profile allowed us to model a single X-ray SLD across an entire POEM/salt domain and assume that spatial variations in X-ray SLD were due to mixing between PS and POEM/salt rather than changes in salt concentration within a POEM domain. Therefore, the combined NR and XRR studies were necessary to quantitatively probe the polymer and salt distributions within the BP.

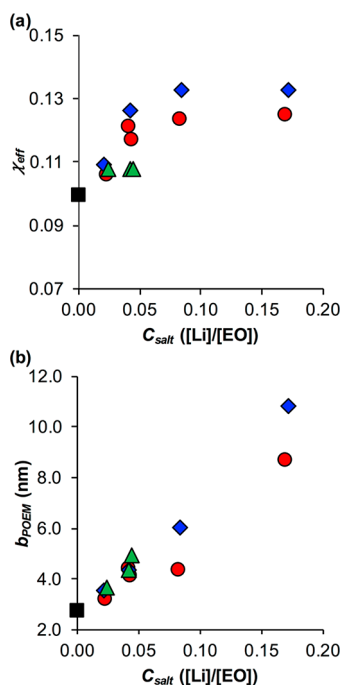


Figure 6. (a) Effective Flory–Huggins interaction parameter (χ_{eff}) and (b) the POEM statistical segment length (b_{POEM}) as a function of C_{salt} . Specimens doped with LiTFSI are plotted with green triangles, specimens doped with Li triflate are plotted with red circles, and specimens doped with Li perchlorate are plotted with blue diamonds.

CONCLUSIONS

We quantitatively examined both the lithium salt and polymer distributions in lithium salt-doped PS-*b*-POEM thin films, and we explored how the presence of salt affects BP chain conformations and thermodynamics. With respect to the lithium salt distribution, analysis of NR data suggested that all salt-doped BP specimens exhibited lithium salt distributions that were directly proportional with the local POEM concentration, a conclusion supported by the lack of even-order Bragg peaks that would result from scattering from salt-rich (centrally localized) layers. By establishing the salt profiles in the BP, polymer interfacial profiles, as determined by XRR, were analyzed with the aid of strong-segregation theory to extract and deconvolute key BP parameters. More specifically, strong-segregation theory was used to calculate both the effective Flory–Huggins interaction parameters and the POEM statistical segment lengths as a function of salt concentration. Our studies indicated that the segregation strength increased at low salt concentrations before plateauing at higher concentrations, while the statistical segment length increased linearly for all tested concentrations. Taken together, these insights can

be harnessed to design new BP materials with tunable domain structure, chain conformation, and segregation strength, providing new routes toward improved BPs for lithium-ion battery electrolyte applications or other BP/dopant systems.

ASSOCIATED CONTENT

Supporting Information

The Supporting Information is available free of charge on the ACS Publications website at DOI: 10.1021/acs.macromol.7b02600.

Contrast match point calculations for PS-*b*-POEM films doped with LiTFSI, Li triflate, and Li perchlorate; NR profiles and multilayer lamellae model fits for PS-*b*-POEM films doped with Li triflate and Li perchlorate; average SLD contrast between PS and POEM/salt as a function of salt concentration; XRR profiles and fits; AFM images of the top surface of select films; polymer volume fraction profiles centered on the PS domain; PS and POEM/salt mass densities obtained from XRR; SST expressions and calculation procedures; a comparison of different methods to calculate χ_{eff} (PDF)

AUTHOR INFORMATION

Corresponding Author

*E-mail: thepps@udel.edu (T.H.E.).

ORCID

Thomas E. Gartner III: 0000-0003-0815-1930

Melody A. Morris: 0000-0001-5597-154X

Cameron K. Shelton: 0000-0001-9172-4394

Thomas H. Epps III: 0000-0002-2513-0966

Author Contributions

T.E.G., M.A.M., and C.K.S. contributed equally to this work.

Notes

The authors declare no competing financial interest.

ACKNOWLEDGMENTS

The NR experiments were conducted under cooperative agreement 70NANB12H239 from NIST, U.S. Department of Commerce, and that agreement also partially supported C.K.S. M.A.M. and T.H.E. acknowledge a Department of Energy grant (DOE BES (DE-SC0014458)) for polymer synthesis and characterization. T.E.G., C.K.S., and T.H.E. thank the National Science Foundation grants (NSF DMR-1207041 and NSF DMR-1610134) for supporting the film preparation and XRR efforts. This AFM facility was supported by the Delaware COBRE program, with a grant from the National Institute of General Medical Sciences – NIGMS (5 P30 GM110758-02) from the National Institutes of Health (NIH). T.H.E. also thanks the Thomas & Kipp Gutshall Professorship for financial support. The statements, findings, conclusions, and recommendations are those of the authors and do not necessarily reflect the views of NIST, the U.S. Department of Commerce, or the NSF. Certain commercial equipment, instruments, materials, suppliers, or software are identified in this paper to facilitate understanding and interpretation of data. Such identifications do not imply recommendation or endorsement by NIST, NSF, DOE, or NIH, nor do they imply that the materials or equipment identified are necessarily the best available for the purpose.

REFERENCES

- (1) Armand, M.; Tarascon, J. M. Building Better Batteries. *Nature* **2008**, *451*, 652–657.
- (2) Bouchet, R.; Maria, S.; Meziane, R.; Aboulaich, A.; Lienafa, L.; Bonnet, J. P.; Phan, T. N. T.; Bertin, D.; Gimes, D.; Devaux, D.; Denoyel, R.; Armand, M. Single-ion BAB Triblock Copolymers as Highly Efficient Electrolytes for Lithium-Metal Batteries. *Nat. Mater.* **2013**, *12* (5), 452–457.
- (3) Xu, W.; Wang, J. L.; Ding, F.; Chen, X. L.; Nasybulin, E.; Zhang, Y. H.; Zhang, J. G. Lithium Metal Anodes for Rechargeable Batteries. *Energy Environ. Sci.* **2014**, *7* (2), 513–537.
- (4) Tarascon, J. M.; Armand, M. Issues and challenges facing rechargeable lithium batteries. *Nature* **2001**, *414* (6861), 359–367.
- (5) Goodenough, J. B.; Park, K. S. The Li-Ion Rechargeable Battery: A Perspective. *J. Am. Chem. Soc.* **2013**, *135* (4), 1167–1176.
- (6) Arora, P.; Zhang, Z. M. Battery separators. *Chem. Rev.* **2004**, *104* (10), 4419–4462.
- (7) Harry, K. J.; Hallinan, D. T.; Parkinson, D. Y.; MacDowell, A. A.; Balsara, N. P. Detection of Subsurface Structures Underneath Dendrites Formed on Cycled Lithium Metal Electrodes. *Nat. Mater.* **2014**, *13* (1), 69–73.
- (8) Hallinan, D. T.; Balsara, N. P. Polymer Electrolytes. *Annu. Rev. Mater. Res.* **2013**, *43*, 503–525.
- (9) Muench, S.; Wild, A.; Friebe, C.; Haupler, B.; Janoschka, T.; Schubert, U. S. Polymer-Based Organic Batteries. *Chem. Rev.* **2016**, *116* (16), 9438–9484.
- (10) Young, W. S.; Kuan, W. F.; Epps, T. H., III Block Copolymer Electrolytes for Rechargeable Lithium Batteries. *J. Polym. Sci., Part B: Polym. Phys.* **2014**, *52* (1), 1–16.
- (11) Morris, M. A.; An, H.; Lutkenhaus, J. L.; Epps, T. H., III Harnessing the Power of Plastics: Nanostructured Polymer Systems in Lithium-Ion Batteries. *ACS Energy Lett.* **2017**, *2* (8), 1919–1936.
- (12) Morris, M. A.; Gartner, T. E., III; Epps, T. H., III Tuning block polymer structure, properties, and processability for the design of efficient nanostructured materials systems. *Macromol. Chem. Phys.* **2017**, *218* (5), 1600513.
- (13) Diederichsen, K. M.; McShane, E. J.; McCloskey, B. D. Promising Routes to a High Li⁺ Transference Number Electrolyte for Lithium Ion Batteries. *ACS Energy Lett.* **2017**, *2* (11), 2563–2575.
- (14) Singh, M.; Odusanya, O.; Wilmes, G. M.; Eitouni, H. B.; Gomez, E. D.; Patel, A. J.; Chen, V. L.; Park, M. J.; Fragouli, P.; Iatrou, H.; Hadjichristidis, N.; Cookson, D.; Balsara, N. P. Effect of Molecular Weight on the Mechanical and Electrical Properties of Block Copolymer Electrolytes. *Macromolecules* **2007**, *40* (13), 4578–4585.
- (15) Panday, A.; Mullin, S.; Gomez, E.; Wanakule, N.; Chen, V.; Hexemer, A.; Pople, J.; Balsara, N. Effect of Molecular Weight and Salt Concentration on Conductivity of Block Copolymer Electrolytes. *Macromolecules* **2009**, *42* (13), 4632–4637.
- (16) Gray, F. M.; Maccallum, J. R.; Vincent, C. A.; Giles, J. R. M. Novel polymer electrolytes based on ABA block copolymers. *Macromolecules* **1988**, *21* (2), 392–397.
- (17) Soo, P. P.; Huang, B. Y.; Jang, Y. I.; Chiang, Y. M.; Sadoway, D. R.; Mayes, A. M. Rubbery block copolymer electrolytes for solid-state rechargeable lithium batteries. *J. Electrochem. Soc.* **1999**, *146* (1), 32–37.
- (18) Ruzette, A. V. G.; Soo, P. P.; Sadoway, D. R.; Mayes, A. M. Melt-formable block copolymer electrolytes for lithium rechargeable batteries. *J. Electrochem. Soc.* **2001**, *148* (6), A537–A543.
- (19) Bates, F. S.; Fredrickson, G. H. Block copolymers - Designer soft materials. *Phys. Today* **1999**, *52* (2), 32–38.
- (20) Bates, F. S.; Hillmyer, M. A.; Lodge, T. P.; Bates, C. M.; Delaney, K. T.; Fredrickson, G. H. Multiblock Polymers: Panacea or Pandora's Box? *Science* **2012**, *336* (6080), 434–440.
- (21) Matsen, M. W. Effect of Architecture on the Phase Behavior of AB-Type Block Copolymer Melts. *Macromolecules* **2012**, *45* (4), 2161–2165.
- (22) Bates, F. S.; Fredrickson, G. H. Block copolymer thermodynamics - Theory and experiment. *Annu. Rev. Phys. Chem.* **1990**, *41*, 525–557.
- (23) Sethuraman, V.; Mogurampelly, S.; Ganesan, V. Multiscale Simulations of Lamellar PS-PEO Block Copolymers Doped with LiPF₆ Ions. *Macromolecules* **2017**, *50* (11), 4542–4554.
- (24) Gomez, E. D.; Panday, A.; Feng, E. H.; Chen, V.; Stone, G. M.; Minor, A. M.; Kisielowski, C.; Downing, K. H.; Borodin, O.; Smith, G. D.; Balsara, N. P. Effect of Ion Distribution on Conductivity of Block Copolymer Electrolytes. *Nano Lett.* **2009**, *9* (3), 1212–1216.
- (25) Gilbert, J. B.; Luo, M.; Shelton, C. K.; Rubner, M. F.; Cohen, R. E.; Epps, T. H., III Determination of lithium-ion distributions in nanostructured block polymer electrolyte thin films by X-ray photoelectron spectroscopy depth profiling. *ACS Nano* **2015**, *9* (1), 512–520.
- (26) Nakamura, I.; Wang, Z. G. Salt-doped block copolymers: ion distribution, domain spacing and effective chi parameter. *Soft Matter* **2012**, *8* (36), 9356–9367.
- (27) Qin, J.; de Pablo, J. J. Ordering Transition in Salt-Doped Diblock Copolymers. *Macromolecules* **2016**, *49* (9), 3630–3638.
- (28) Chintapalli, M.; Le, T. N. P.; Venkatesan, N. R.; Mackay, N. G.; Rojas, A. A.; Thelen, J. L.; Chen, X. C.; Devaux, D.; Balsara, N. P. Structure and Ionic Conductivity of Polystyrene-block-poly(ethylene oxide) Electrolytes in the High Salt Concentration Limit. *Macromolecules* **2016**, *49* (5), 1770–1780.
- (29) Chandrashekar, S.; Oparaji, O.; Yang, G.; Hallinan, D. Communication-Li-7 MRI Unveils Concentration Dependent Diffusion in Polymer Electrolyte Batteries. *J. Electrochem. Soc.* **2016**, *163* (14), A2988–A2990.
- (30) Young, W. S.; Epps, T. H., III Salt doping in PEO-containing block copolymers: counterion and concentration effects. *Macromolecules* **2009**, *42* (7), 2672–2678.
- (31) Wanakule, N. S.; Panday, A.; Mullin, S. A.; Gann, E.; Hexemer, A.; Balsara, N. P. Ionic Conductivity of Block Copolymer Electrolytes in the Vicinity of Order-Disorder and Order-Order Transitions. *Macromolecules* **2009**, *42* (15), 5642–5651.
- (32) Wanakule, N. S.; Virgili, J. M.; Teran, A. A.; Wang, Z. G.; Balsara, N. P. Thermodynamic Properties of Block Copolymer Electrolytes Containing Imidazolium and Lithium Salts. *Macromolecules* **2010**, *43* (19), 8282–8289.
- (33) Wang, J. Y.; Chen, W.; Russell, T. P. Ion-complexation-induced changes in the interaction parameter and the chain conformation of PS-b-PMMA copolymers. *Macromolecules* **2008**, *41* (13), 4904–4907.
- (34) Wang, Z. G. Effects of Ion Solvation on the Miscibility of Binary Polymer Blends. *J. Phys. Chem. B* **2008**, *112* (50), 16205–16213.
- (35) Nakamura, I.; Wang, Z. G. Thermodynamics of Salt-Doped Block Copolymers. *ACS Macro Lett.* **2014**, *3* (8), 708–711.
- (36) Teran, A. A.; Balsara, N. P. Thermodynamics of block copolymers with and without salt. *J. Phys. Chem. B* **2014**, *118* (1), 4–17.
- (37) Gunkel, I.; Thurn-Albrecht, T. Thermodynamic and Structural Changes in Ion-Containing Symmetric Diblock Copolymers: A Small-Angle X-ray Scattering Study. *Macromolecules* **2012**, *45* (1), 283–291.
- (38) Wang, J. Y.; Leiston-Belanger, J. M.; Sievert, J. D.; Russell, T. P. Grain rotation in ion-complexed symmetric diblock copolymer thin films under an electric field. *Macromolecules* **2006**, *39* (24), 8487–8491.
- (39) Semenov, A. N. Contribution To The Theory Of Microphase Layering In Block-Copolymer Melts. *Zhurnal Eksperimentalnoi I Teoreticheskoi Fiziki* **1985**, *88* (4), 1242–1256.
- (40) Semenov, A. N. Microphase Separation In Diblock Copolymer Melts - Ordering Of Micelles. *Macromolecules* **1989**, *22* (6), 2849–2851.
- (41) Matsen, M. W.; Bates, F. S. Unifying weak- and strong-segregation block copolymer theories. *Macromolecules* **1996**, *29* (4), 1091–1098.
- (42) Lipic, P. M.; Bates, F. S.; Matsen, M. W. Non-equilibrium phase behavior of diblock copolymer melts and binary blends in the intermediate segregation regime. *J. Polym. Sci., Part B: Polym. Phys.* **1999**, *37* (16), 2229–2238.
- (43) Matsen, M. W.; Bates, F. S. Conformationally asymmetric block copolymers. *J. Polym. Sci., Part B: Polym. Phys.* **1997**, *35* (6), 945–952.

- (44) Huang, J.; Tong, Z. Z.; Zhou, B.; Xu, J. T.; Fan, Z. Q. Salt-induced microphase separation in poly(epsilon-caprolactone)-b-poly(ethylene oxide) block copolymer. *Polymer* **2013**, *54* (12), 3098–3106.
- (45) Nakamura, I.; Balsara, N. P.; Wang, Z. G. Thermodynamics of Ion-Containing Polymer Blends and Block Copolymers. *Phys. Rev. Lett.* **2011**, *107* (19), 198301.
- (46) Pynn, R. Neutron Scattering-A Non-destructive Microscope for Seeing Inside Matter. *Neutron Applications in Earth, Energy and Environmental Sciences* **2009**, 15–36.
- (47) Svergun, D. I.; Feigin, L. A.; Taylor, G. W. *Structure Analysis by Small-Angle X-ray and Neutron Scattering*; Plenum Press: New York, 1987.
- (48) Lodge, T. P.; Hamersky, M. W.; Hanley, K. J.; Huang, C. I. Solvent distribution in weakly-ordered block copolymer solutions. *Macromolecules* **1997**, *30* (20), 6139–6149.
- (49) Virgili, J. M.; Nedoma, A. J.; Segalman, R. A.; Balsara, N. P. Ionic Liquid Distribution in Ordered Block Copolymer Solutions. *Macromolecules* **2010**, *43* (8), 3750–3756.
- (50) Broseta, D.; Leibler, L.; Kaddour, L. O.; Strazielle, C. A theoretical and experimental study of interfacial-tension of immiscible polymer blends in solution. *J. Chem. Phys.* **1987**, *87* (12), 7248–7256.
- (51) Tsarevsky, N. V.; Sumerlin, B. S.; Matyjaszewski, K. Step-growth “click” coupling of telechelic polymers prepared by atom transfer radical polymerization. *Macromolecules* **2005**, *38* (9), 3558–3561.
- (52) Kuan, W. F.; Reed, E. H.; Nguyen, N. A.; Mackay, M. E.; Epps, T. H., III Using tapered interfaces to manipulate nanoscale morphologies in ion-doped block polymers. *MRS Commun.* **2015**, *5* (2), 251–256.
- (53) Stafford, C. M.; Roskov, K. E.; Epps, T. H., III; Fasolka, M. J. Generating thickness gradients of thin polymer films via flow coating. *Rev. Sci. Instrum.* **2006**, *77* (2), 023908.
- (54) Dura, J. A.; Pierce, D. J.; Majkrzak, C. F.; Maliszewskij, N. C.; McGillivray, D. J.; Losche, M.; O'Donovan, K. V.; Mihailescu, M.; Perez-Salas, U.; Worcester, D. L.; White, S. H. AND/R: Advanced neutron diffractometer/reflectometer for investigation of thin films and multilayers for the life sciences. *Rev. Sci. Instrum.* **2006**, *77* (7), 074301–074301–11.
- (55) DeCaluwe, S. C.; Kienzle, P. A.; Bhargava, P.; Baker, A. M.; Dura, J. A. Phase segregation of sulfonate groups in Nafion interface lamellae, quantified via neutron reflectometry fitting techniques for multi-layered structures. *Soft Matter* **2014**, *10* (31), 5763–5776.
- (56) Kienzle, P. A.; O'Donovan, K. V.; Ankner, J. F.; Berk, N. F.; Majkrzak, C. F. <http://www.ncnr.nist.gov/reflpak>, 2000–2006.
- (57) Dura, J. A.; Rus, E. D.; Kienzle, P. A.; Maranville, B. B. Nanolayer Analysis by Neutron Reflectometry. In *Nanolayer Research: Methodology and Technology for Green Chemistry*; Imae, T., Ed.; Elsevier: Amsterdam, 2017; pp 155–202.
- (58) Sears, V. F. Neutron scattering lengths and cross sections. *Neutron News* **1992**, *3* (3), 26–37.
- (59) Saxena, A. M.; Schoenborn, B. P. Multilayer Neutron Monochromators. *Acta Crystallogr., Sect. A: Cryst. Phys., Diffraction, Theor. Gen. Crystallogr.* **1977**, *33*, 805–813.
- (60) Metwalli, E.; Nie, M.; Körstgens, V.; Perlich, J.; Roth, S. V.; Müller-Buschbaum, P. Morphology of Lithium-Containing Diblock Copolymer Thin Films. *Macromol. Chem. Phys.* **2011**, *212* (16), 1742–1750.
- (61) Epps, T. H., III; Bailey, T. S.; Waletzko, R.; Bates, F. S. Phase behavior and block sequence effects in lithium perchlorate-doped poly(isoprene-b-styrene-b-ethylene oxide) and poly(styrene-b-isoprene-b-ethylene oxide) triblock copolymers. *Macromolecules* **2003**, *36* (8), 2873–2881.
- (62) Luo, M.; Brown, J. R.; Remy, R. A.; Scott, D. M.; Mackay, M. E.; Hall, L. M.; Epps, T. H., III Determination of Interfacial Mixing in Tapered Block Polymer Thin Films: Experimental and Theoretical Investigations. *Macromolecules* **2016**, *49* (14), 5213–5222.
- (63) Anastasiadis, S. H.; Russell, T. P.; Satija, S. K.; Majkrzak, C. F. The morphology of symmetric diblock copolymers as revealed by neutron reflectivity. *J. Chem. Phys.* **1990**, *92* (9), 5677–5691.
- (64) Gartner, T. E., III; Kubo, T.; Seo, Y.; Tansky, M.; Hall, L. M.; Sumerlin, B. S.; Epps, T. H., III Domain Spacing and Composition Profile Behavior in Salt-Doped Cyclic vs Linear Block Polymer Thin Films: A Joint Experimental and Simulation Study. *Macromolecules* **2017**, *50* (18), 7169–7176.
- (65) Russell, T. P.; Hjelm, R. P.; Seeger, P. A. Temperature-dependence of the interaction parameter of polystyrene and poly(methyl methacrylate). *Macromolecules* **1990**, *23* (3), 890–893.
- (66) Helfand, E.; Tagami, Y. Theory of interface between immiscible polymers. II. *J. Chem. Phys.* **1972**, *56* (7), 3592–3601.
- (67) Broseta, D.; Fredrickson, G. H.; Helfand, E.; Leibler, L. Molecular-weight and polydispersity effects at polymer polymer interfaces. *Macromolecules* **1990**, *23* (1), 132–139.
- (68) Ishizone, T.; Han, S.; Hagiwara, M.; Yokoyama, H. Synthesis and surface characterization of well-defined amphiphilic block copolymers containing poly[oligo(ethylene glycol) methacrylate] segments. *Macromolecules* **2006**, *39* (3), 962–970.